Macro and Micro Scale Load Effects on Tribocorrosion Mechanisms in Biomedical CoCrMo Alloys

E.Hyla[a,*], A. R. Beadling[b], G. de Boer[a], R. M. Hall[b], M. G. Bryant[b]

[a]*School of Mechanical Engineering, University of Leeds, Leeds, LS2 9JT, UK*
[b]*School of Engineering, University of Birmingham, Birmingham, B15 2TT,UK*

Abstract

Understanding wear mechanisms is crucial for enhancing the durability and effectiveness of joint implants. Despite advances in the field, a gap persists in connecting different length scales, tribocorrosion, and overall debris formation, underscoring the need for enhancements.

This study investigates the degradation process of the low-carbon cobaltchromiummolybdenum alloy, examining its behaviour across macro and micro scales. The coefficient of friction (COF) was shown to be influenced by initial contact pressures, alongside a transition from predominantly mechanical to mainly corrosive wear when shear stresses in the contact fell below the shear strength of the bulk.

By integrating insights from both scales, this study provides a comprehensive perspective on wear processes. It contributes to the development design strategies and further improved material performance.

Keywords: Tribocorrosion, Friction, Wear, CoCrMo Alloy

1. Introduction

The release of metal particles from biomedical implants has been widely studied due to its role in inflammatory responses and implant failure. Fretwurst et al. [1] identified metal particles in peri-implant supporting tissues, raising concerns about their potential contribution to both local and systemic inflammation. Research suggests that wear debris and ion release negatively affect periprosthetic tissue reactions, leading to aseptic loosening and implant failure [2]. Additionally, in the context of systemic toxicity, Chang et al. [3] reported a 5.3% incidence of metallosis in total hip replacements. Given that the global hip replacement market is projected to reach $11.59 billion by 2032 [4], a comprehensive understanding of bio-tribocorrosion mechanisms is essential for enhancing the longevity and reliability of biomedical implants.

Tribocorrosion, the combined effect of mechanical wear and corrosion, plays a critical role in the degradation and longevity of biomedical implants [5; 6]. The performance and durability of biomedical alloys are significantly affected by synergistic interactions between these factors [7].

*Corresponding author
Email addresses: mn17eh@leeds.ac.uk (E.Hyla), m.g.bryant@bham.ac.uk (M. G. Bryant)

Wimmer et al. [8] conducted a study on recovered hip joints. The study revealed the formation of a tribocorrosive layer through a process they named mechanical mixing. Furthermore, this nanocrystalline layer was related to the generation of wear particles and their subsequent detachment into the surrounding tissue from adhesion-dominated wear mechanisms.

Building on this foundation, Fischer et al. [9] studied various biomaterials and their microstructure changes, with the aim of establishing connections with wear formation . The study concluded the importance of subsurface mechanical behaviour, particularly cyclic creep and dislocation formation, in determining the long-term wear performance of materials in biomedical implants. However, a significant limitation of their investigation lay in the omission of lubrication and corrosion considerations, since the tests were performed under dry conditions [9].

Subsequent studies addressed these limitations through the use of joint simulators that replicate in vivo conditions [10]. Although these studies are very important in simulating the biomechanics of the human body, they remain simplified representations of surface interactions at the asperity level. On a microscopic scale, interactions transpire among surface asperities, which induce elevated stresses. Statistical theories of asperity contact have been proposed in the literature [11; 12], starting from the studies of Greenwood et al. [13] to novel deterministic approach for calculating the electrochemical current in tribocorrosive wear environments [14]. However, their experimental application to biomaterials is still limited.

Recent studies have started to explore aspects of multi-scale tribocorrosion. For example, Brazil et al. [15] demonstrated that microscopic features such as plastic sink-in significantly influence static friction in single asperity contacts, highlighting the role of micro-scale contact mechanics in shaping macro-scale tribological behaviour. Ghanbarzadeh et al. [14] combined electrochemical simulations with asperity-level contact mechanics to model the coupled effects of wear and corrosion, offering detailed insight into localised degradation mechanisms. Mace and Gilbert [16] further investigated the tribocorrosive response of metals using an idealised single-asperity setup, examining the combined effects of potential difference, mechanical load, and cycle number.

However, despite these contributions, there remains a lack of evidence directly linking scale-dependent interactions to material degradation pathways. While many studies have investigated either micro- or macro-scale tribocorrosion independently, to the best of our knowledge, no existing work has experimentally examined both scales within a single framework to compare their effects and establish a direct connection between them.

This gap limits our understanding of how tribocorrosion mechanisms evolve across different contact conditions and prevents a unified view of degradation behaviour in biomedical alloys. Further, since debris generation is a direct outcome of material degradation, an incomplete understanding of tribocorrosion across scales restricts our ability to anticipate its clinical implications, including inflammatory responses and implant failure.

Consequently, there is a pressing need for enhancements to mitigate these limitations. By understanding

the tribocorrosive behaviour of CoCrMo alloys at different scales, we can potentially translate these findings to inform and improve implant design, enhancing wear and corrosion resistance. Therefore, in this study we designed a multi-scale tribocorrosion approach combining macro- and micro-contact testing using diamond tips of different radii under controlled electrochemical conditions. By COF evolution, wear volume measurements, and morphological changes, with calculated contact pressures and shear stress, we establish the relationship between contact scale, applied stress, and wear mechanism. This integrated methodology enables us to mechanistically map the tribocorrosive behaviour of CoCrMo alloys across scales and identify critical thresholds for wear transitions.

2. Materials and Methodology

2.1. CoCrMo Samples

Co-28Cr-6Mo alloy (CoCrMo)(Oracle, UK), a low-carbon wrought material, with a hardness of 5.2 GPa, manufactured according to ASTM F1537 was employed for tribocorrosion analysis [17]. The elemental composition of CoCrMo as per the suppliers data sheet, adhering to the guidelines outlined in the aforementioned standard, is delineated in Table 1.

Table 1: Composition of Low Carbon CoCrMo according to the suppliers data sheet

Element	C	Mn	Si	Co	Cr	Mo	Ni	Fe
Concentration (%)	0.05	0.8	0.6	Rest	27.7	5.5	0.16	0.28

Supplied as a 10 mm diameter rod, it was cut into a 4 mm thick flat sample. The samples underwent grinding using sequential silicon carbide paper with grit sizes from 600, 800, 1200 and 4000. Subsequently, mirror-polishing was carried out using sequential diamond paste with particle sizes 6 μm, 3 μm, 0.5 μm, and 0.25 μm, further refining the surface and reducing roughness. The mean roughness value R_a for the surface after polishing was measured using vertical scanning interferometry and resulted in around 0.005 μ m which complied with the maximum limit (R_a = 0.05 μm) given by the technical standard ISO 7206-2 (2011/AMD 1:2016) for partial and total hip joint prostheses [18]. Subsequently, the samples were immersed in acetone and subjected to ultrasonic cleaning for a duration of 10 minutes, ensuring the removal of possible contaminants. They were then rinsed with deionised water and dried in a stream of dry air. The prepared CoCrMo samples were then immediately used for tribocorrosion testing.

2.2. Lubricant and test environment

The experiments were conducted at ambient room temperature, with phosphate buffer saline (PBS) solution (Thermo Scientific, UK) as the test medium. These conditions were chosen to eliminate potential confounding factors such as temperature effects and solution reactions, thereby enabling a targeted study

of scale and load effects on wear phenomena. PBS was synthesised prior to the experiments by dissolving a commercially available PBS tablet in 100 mL of deionised water, using a magnetic stirrer to ensure homogeneity. This buffer solution has a stable pH environment as well as the ion concentration and osmolarity which align with physiological levels found in human bodily fluids [19].

2.3. Tribocorrosion tests

A linear-reciprocating nanotribometer (NTR^3) with atomic force microscopy level precision (Anton Paar, UK) was used to investigate the effects of a single asperity scratch behaviour. High-resolution capacitive sensors and a dual quad-beam cantilever with a stiffness of $F_{\mathrm{n}} = 5.504$ mN/μm and $F_{\mathrm{t}} = 12.55$ mN/μm were employed to independently measure normal and friction forces, which ensures changes in one direction do not affect the other [20]. The piezo actuator in the NTR^3 respectively monitored the normal force detected by the sensor and adjusted its position to maintain a stable normal force. This provided it with high precision in measuring nanoscale friction, making it suitable for studying materials at very small scales.

Additionally two counter tips were used to simulate different asperity sizes in contact. The counter tip, which simulates a macro-scale contact, was constructed as a dome-shaped diamond tip with a diameter $D_{\mathrm{tip200}} = 200$ μm (Micro Materials Ltd, UK) providing insight into larger-scale contact behaviour, more representative of bulk material response [21]. In addition to D_{tip200}, a second diamond tip of the same manufacturer, with a diameter $D_{\mathrm{tip25}} = 25$ μm represents interactions on the microscale, where localised deformation and asperity-level mechanics dominate [22]. A range of normal loads ($F_n = 10, 50, 100$, and 200 mN) was applied, resulting in contact pressures ranging from 1.95 to 5.29 GPa for D_{tip200} and 7.79 to 21.15 GPa for D_{tip25}. The actual contact area between two metal surfaces is significantly smaller than the apparent contact area due to surface roughness [23]. This leads to extremely high localised pressures at asperity contact points, even when the overall contact pressure remains low [24]. Previous studies investigating nano-fretting and reciprocating sliding wear in CoCrMo alloys have reported contact pressures ranging from 0.77 to 21 GPa [25]. Therefore, the test conditions employed in this study were designed to reflect clinically relevant contact pressures at the asperity level within modular hip joint components.

To enhance electrical isolation and prevent interference, the tip holder made from stainless steel was further coated with a layer of Acrylic Protective Lacquer (Electrolube, UK). This coating served to minimise the potential for unwanted reactions from the tip holder during the tribocorrosion experiments, ensuring the integrity of the measurements and the accuracy of the results.

The mean values of COF recorded during reciprocate sliding were plotted against cycles for further analysis. To be able to probe the currents at the nA range a sliding motion was performed with a reciprocating stroke length of 1.5 mm at 1.5 Hz for 30 min. The experiments were performed with a total of three replicates (n = 3) for each test condition.The results presented in the study represent the mean values obtained from these three independent trials. To assess the repeatability and variability of the data, standard deviations were calculated and are provided alongside the mean values in the relevant figures and tables.

2.4. Corrosion Study

To examine the impact of corrosion during sliding, a sample holder shown in Figure 1 was designed and integrated on the nanotribometer which enabled integration of a three-electrode electrochemical cell. This sample holder allowed immersion of the sample in a liquid environment. The holder consisted of two parts: an aluminium component facilitated the working electrode connection to the 10 mm CoCr plate, and a polyether ether ketone (PEEK) component which clamped the CoCr sample within the holder and restricted the exposed surface area of the sample to a diameter of 5 mm. To ensure a leak-proof seal within this restricted area, a perfluoroelastomer (FFKM) O-ring with dynamic sealing capability was employed.

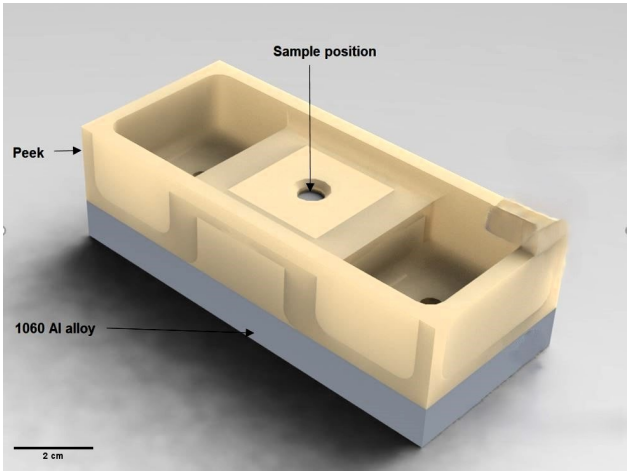

Figure 1: The image shows a tribocorrosion bath with a PEEK top section and an aluminum alloy base. The PEEK limits the exposed sample area to 5 mm. The design ensures electrical isolation while providing a stable connection for tribocorrosion testing.

Inside the bath, a three-electrode cell was used. An Orion Redox ORP Electrode (ThermoFisher Scientific, UK) with a Silver/Silver-Chloride (Ag/AgCl) reference electrode and a Platinum (Pt) counter electrode was used to generate electrical currents. A schematic of the tribocorrosion set up is shown in Figure 2a

A compactstat (Ivium Technologies, NL) was used to apply controlled voltages via Ivium Soft (Ivium Technologies, NL) where chronoamperometry measurements were performed. Current transients were recorded under potentiostatic polarisation conditions (+100mV vs Ag/AgCl). This current value has been demonstrated to induce a shift in the material towards the passivation region [26]. The current changes were recorded as a function of time at a rate of $0.1\,s^{-1}$.

Firstly, the tip is loaded onto the surface by applying 95% of the intended normal load. Following this, the system was allowed to stabilise which was characterised by an exponential decay in anodic current; linked to passive film growth [27]. The equipment was then fully loaded to the predetermined set load, and reciprocating sliding was executed for an additional 30 minutes, which is equivalent to a total of 2700 cycles. At the start of sliding, an increase in current was observed due to depassivation and exposure of the reactive nascent substrate to the lubricant. After the completion of the sliding, the current decreased

due to repassivation [27]. A subsequent 30-minute monitoring period was then implemented to evaluate the recovery and passivation of the contact. An example of the output is shown in Figure 2b

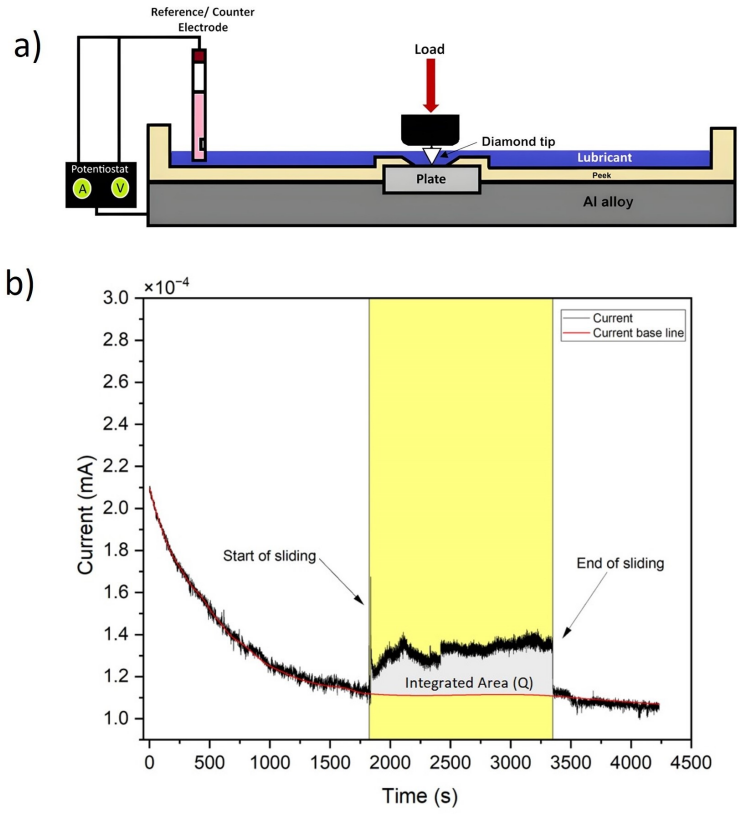

Figure 2: a) Tribocorrosion schematic. b) Example of changes in current induced by mechanical wear caused by the Diamond Tip scratching the surface of the mechanically polished CoCrMo sample

2.5. Theory and calculations

2.5.1. Hamrock-Dowson Minimum Lubricant Film Thickness

In tribological systems, the formation and stability of a lubricating film are critical in determining the extent of surface separation and the dominant wear mechanisms. For point or elliptical contacts, the Hamrock-Dowson equations provide a well-established analytical model to estimate the minimum lubricant film thickness under elastohydrodynamic lubrication (EHL) conditions [28]. These equations incorporate the effects of speed, material properties, load, and contact geometry through dimensionless parameters. Applying this model allows for the quantification of film thickness and, subsequently, the estimation of the lubrication regime using the dimensionless Lambda Λ -ratio [28]. This framework is essential for understanding whether contact occurs predominantly in a full film, mixed, or boundary lubrication state, which directly influences tribocorrosion performance.

The minimum film thickness $h_{\min}$ is given by:

$$h_{\min} = 3.63\, U^{0.68}\, G^{0.49}\, W^{-0.073}\, R \tag{1}$$

where U is the dimensionless speed parameter, G is the dimensionless material parameter, W is the dimensionless load parameter, and R is the tip radius.

The dimensionless speed parameter U is defined as:

$$U = \frac{\eta_0 u}{E' R} \tag{2}$$

Here, η_0, is the dynamic viscosity of the lubricant, u, is the average sliding velocity, and E', is the reduced elastic modulus.

The reduced elastic modulus E' is given by:

$$\frac{1}{E'} = \frac{1-\nu_1^2}{E_1} + \frac{1-\nu_2^2}{E_2} \tag{3}$$

where E_1 and E_2 are the Youngs moduli, and ν_1 and ν_2 are the Poissons ratios of the respective materials. The above is calculated for a dome-shaped Diamond tip with $E_1 = 1050$ GPa and $\nu_1 = 0.2$ and a flat CoCrMo surface with $E_2 = 220$ GPa and $\nu_2 = 0.29$.

The material parameter G is defined as:

$$G = \alpha_p E' \tag{4}$$

where α_p, is the pressureviscosity coefficient of the lubricant.

Finally, the load parameter W is defined as:

$$W = \frac{F_n}{E' R^2} \tag{5}$$

The lubrication regime is then determined using the following equation:

$$\Lambda = \frac{h_{\min}}{\sigma} \tag{6}$$

where the combined surface roughness σ is calculated from the roughness of the CoCrMo surface σ_1 and the diamond tip σ_2 using:

$$\sigma = \sqrt{\sigma_1^2 + \sigma_2^2} \tag{7}$$

Following the classification of lubrication regimes:

$\Lambda > 3$ Full Film Lubrication

$1 < \Lambda \leq 3$ Mixed Lubrication

$\Lambda < 1$ Boundary Lubrication

2.5.2. Mechanistic aproach

In the context of quantifying material loss mechanisms, the mechanistic approach offers a systematic framework to break down tribocorrosion into its constituent components of mechanical induced wear, (V_{mech}) and corrosive wear loss, (V_{chem}) and analyse each factor's contribution quantitatively [29]. According to this method the total volume loss, (V_{total}) is equal to:

$$V_{\mathrm{total}} = V_{\mathrm{chem}} + V_{\mathrm{mech}} \tag{8}$$

Further, V_{total} is measured using profilometry (VSI, NPFlex TM, Bruker, US) while V_{chem} in a potentiostatic tribocorrosion experiment can be determined from the measured current using Faradays law:

$$V_{\mathrm{chem}} = \frac{QM}{nF\rho} \tag{9}$$

Where Q is the electric charge obtained by integrating the measured current over the time of the experiment [29]. Faradays constant (F) was taken as 96,500 C/mol, and the molar mass (M) was 55.7 g/mole, reflecting the stoichiometric mean of the CoCrMo alloys composition. Consequently, the valence number (n) was assumed to be 2.4, with a material density (ρ) of 8.29 g/cm^3. These parameters align with those adopted in preceding investigations involving CoCrMo specimens [30].

2.5.3. Hertzian Contact Theory, Shear Sresses and Degree of Penetration

For contact mechanics analysis Hertzian contact theory has been used to calculate initial contacting pressure [31].

The maximum contact pressure for a sphere on a plane is calculated by:

$$p_{\mathrm{max}} = \frac{1}{\pi}\left(\frac{6F_n E'}{R^2}\right)^{1/3} \tag{10}$$

Furthermore, the shear stress (τ_c) in the contact area can be related to p_{max} through the Hertzian contact theory. It can be approximated that the shear stress τ_c is half of the normal contact pressure:

$$\tau_c = \frac{p_{\mathrm{max}}}{2} \tag{11}$$

Moreover, the maximum yield shear strength of the material was acquired from the material dataset provided by the supplier and was equal to τ_0=0.86 GPa. Further, the Tresca criterion was applied to determine if the material would yield under these conditions [32]. In addition to identify the wear mechanisms the wear map for ductile metals was used by normalising the critical shear strength/stress values[33]:

$$\tau = \frac{\tau_0}{\tau_c} \tag{12}$$

and calculate the degree of penetration (D_p):

$$D_p = \frac{h}{a} \tag{13}$$

where h is the penetration depth and is equal to:

$$h = \frac{a^2}{R} \tag{14}$$

while a is the contact radius and is calculated as:

$$a = \left(\frac{3F_n R}{4E}\right)^{\frac{1}{3}} \tag{15}$$

All the calculated values are shown in Table 2.

Table 2: Calculated results for various parameters including: Radius of initial contacting area (a), Hertzian contact pressure ($p_{\max}$), initial penetration height (h), degree of penetration (D_{p}), and shear stress at the contact between tip and surface (τ_{c}) for different contacting geometries and loads. Also included are values for bulk shear stress (τ_0) from the manufacturer's dataset, along with an indication if the material is yielding according to the Tresca criterion.

Tip Radius (μm)	Load (mN)	Contact Area Radius (μm)	Contact Pressure (GPa)	Initial Penetration Depth (μm)	Degree of Penetration (Dp)	Shear Stress (GPa)	Shear Strength (GPa)	Yielding (Tresca)
100	10.0	1.57	1.95	0.02	0.016	0.97	0.86	YES
100	100.0	3.37	4.20	0.11	0.034	2.1	0.86	YES
100	200.0	4.25	5.29	0.18	0.042	2.64	0.86	YES
12.5	10.0	0.78	7.79	0.05	0.063	3.90	0.86	YES
12.5	50.0	1.34	13.33	0.14	0.107	6.66	0.86	YES
12.5	100.0	1.69	16.79	0.23	0.135	8.39	0.86	YES
12.5	200.0	2.12	21.15	0.36	0.170	10.58	0.86	YES

2.5.4. Archards Law

In cases where no visible wear was observed, Archards law was applied to estimate the potential total wear volume loss (V_{total}) based on the contact conditions.

The wear volume V is given by:

$$V = \frac{KWL}{H} \tag{16}$$

where:

K is the dimensionless wear coefficient,

W is the applied normal load,

L is the total sliding distance,

H is the hardness of the softer material in contact.

2.6. Vertical Scanning Interferometry (VSI)

A Vertical Scanning Interferometer (VSI, NPFlex, Bruker, USA) was employed to capture profiles of the samples, enabling the quantification of total volumetric loss subsequent to sliding tests. The VSI functioned

based on white light interferometry, utilises surface reflections to generate interference fringes. The system operated at 20× magnification with a scanning speed of 1× and achieved a spatial resolution of 0.24 μm. A 3D image with a length of 2 mm and a width of 0.2 mm was recorded. The data acquisition was processed through Vision64 software (Bruker, MA, USA), which facilitated the construction of detailed wear scar profile representations. To determine the wear scar's contour and the negative volume the surface was subtracted from any tilting. Subsequently, the total volume loss was precisely measured by modifying the reference plane height, allowing for an inclusive assessment of all points situated beneath this plane.

2.7. Field Emission Gun - Scanning Electron Microscopy (FEG-SEM)

The FEI Helios G4 CX DualBeam (Thermo Fischer, UK) is used in this study to analyse the morphology of the wear surface. The high-resolution monochromated FEG-SEM generates a focused beam of high-energy electrons using an electron gun, like a standard SEM. The electron beam is directed at the sample under investigation. When the electrons interact with the sample's surface, they produce various signals, including secondary electrons (SEs) and back-scattered electrons (BSEs). To capture the wear scar images the secondary electron detector was chosen due to its high-resolution images of the sample's surface topography.

3. Results and discussion

3.1. Lubrication

For all tested conditions, the calculated values (provided in the supplementary material) confirm that the system remains in the boundary lubrication regime, indicating solid-to-solid contact with an insufficient lubricant film to fully separate the surfaces. As a result, the lubrication does not provide effective protection against wear, and therefore, we neglect the lubrication effects in further considerations.

3.2. Coefficient of friction (COF)

The evolution of the COF over cycles while sliding at each contact pressure for D_{tip200} and D_{tip25} is shown in Figure 3a,b. The initial phase, known as the 'running-in' regime, is marked by surface adaptations between contacting bodies. Notably, Figure 3c and d highlight the running-in regime where a distinct transition in the COF trend between the macro and micro contact is observed.

Under the macro-contact D_{tip200}, the COF initiates at values as low as approximately 0.06, with a subsequent increase to 0.1 observed after 150 cycles. Conversely, at microcontact with D_{tip25}, the COF starts at a higher value around 0.13 initially, but reaches values as low as 0.05 within the first 50 cycles. This occurrence suggests that the changing pressure conditions induce alterations in the materials deformation behaviour at different scales, ultimately influencing its tribological responses during the process.

Following the running-in period, the COF stabilises, entering a steady state and maintaining a relatively consistent value for the remaining duration of the test, regardless of contact scales and loads. Further,an increase of COF with decreasing initial surface pressure, supports findings reported in previous studies [25].

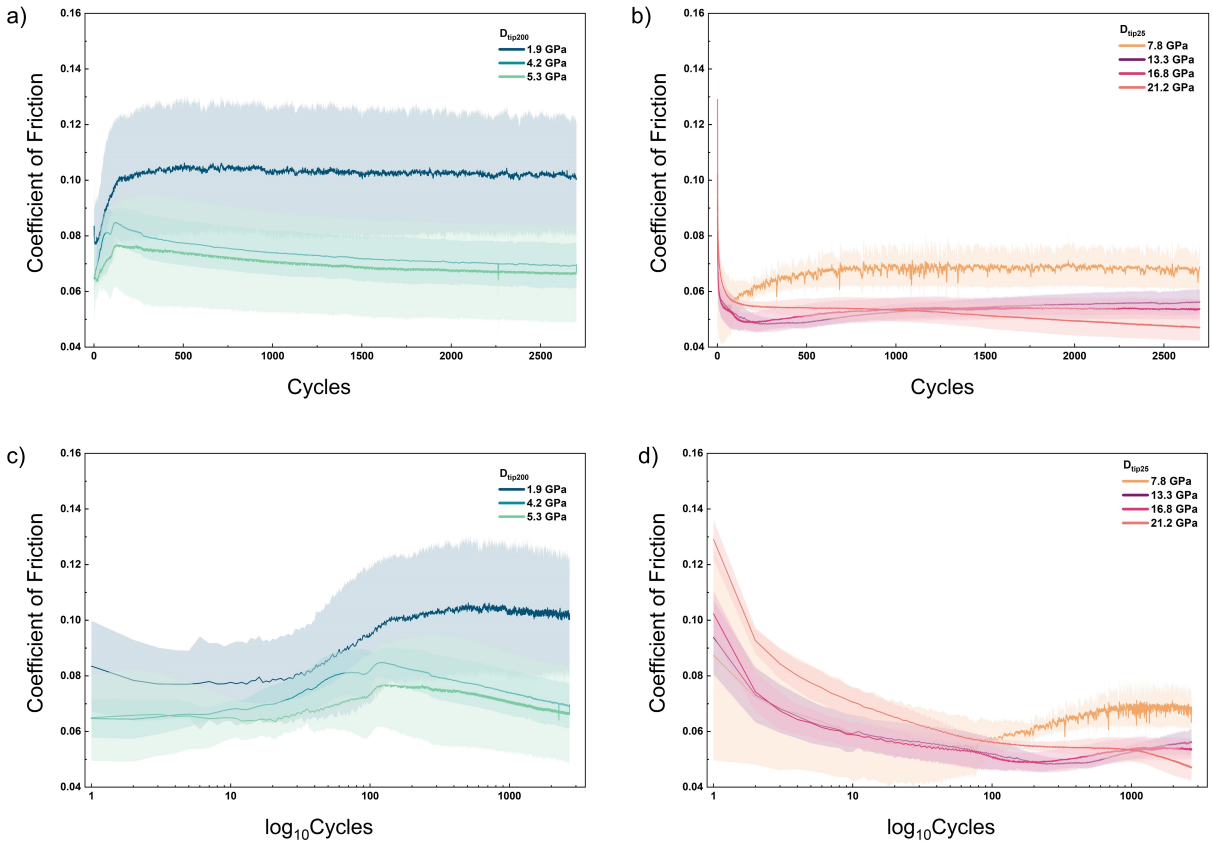

Figure 3: COF evolution over cycles for (a) D_{tip200} and (b) D_{tip25}. (c) A logarithmic representation of COF over cycles highlights the variation in COF behaviour during the running-in phase, demonstrating a change in trend with decreasing contact pressures for D_{tip200}, while (d) shows the corresponding behaviour for D_{tip25}.

One explanation to why this occurs can be found in the adhesion hypothesis proposed by Bowden and Tabor [34]. According to this hypothesis, resistance to relative motion arises from the formation of adhesive bonds between asperity tips when positioned at an interatomic distance. It is known that the COF is recognised to result from the cooperative influence of adhesion and ploughing contributions [35]. However, given the mirror-polished surface and the inherently weak van der Waals/London forces at the interface, it is unlikely that the observed increase in COF results from increased adhesion forces [36]. Instead, the ease with which the tip ploughs the surface at high surface pressures is likely the primary factor contributing to the low COF values.

This correlation is further confirmed by the analysis of wear scar profiles obtained through VSI, as shown in Figure 4a. In these profiles, ploughing becomes less distinct as contact pressure decreases (Figure 4)b. At 21.2 GPa, the height on the side of the wear scar reached 1.5 μm, whereas at 1.9 GPa, it was indistinguishable from the surface roughness. Notably, this reduction in ploughing coincides with an increase in COF, further supporting the link between ploughing and lower COF values.

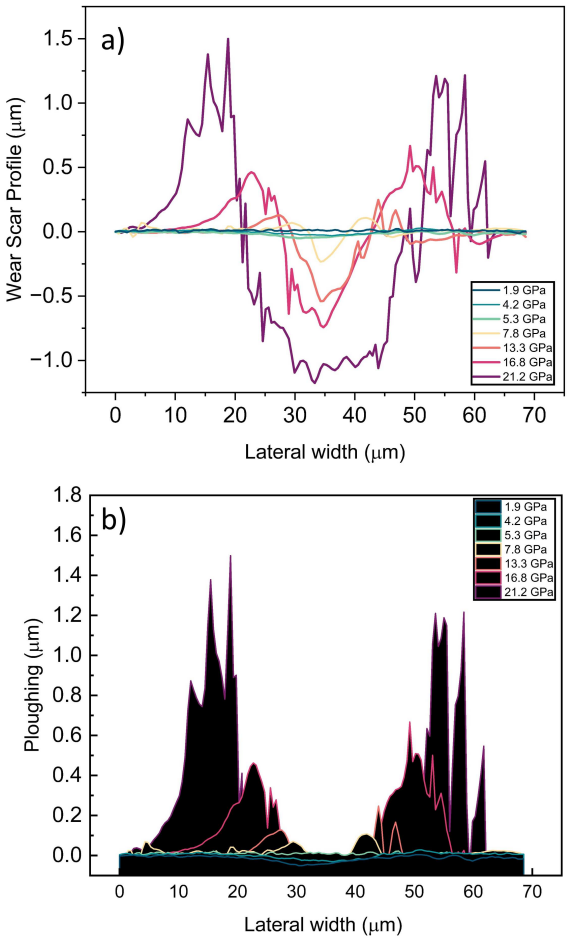

Figure 4: VSI scans depicting a) the final wear scar profiles corresponding to each initial contact pressure, and b) ploughing observed on the side of the wear scar for each initial contact pressure.

A better understanding is obtained by calculating the shear stress from Eq. 11 (Table 2). As the applied shear stress approaches the material's bulk shear strength, consequently, surface asperities effectively withstand sliding, leading to higher transversal forces and a higher COF. Furthermore by calculating the degree of penetration from Eq. 13 and using the abrasive wear map for ductile metals (Figure 5), we can indicate that pure ploughing consistently manifested across all samples besides the samples tested with D_{tip25} under 200 mN where a transition of cutting wear becomes evident. The obtained low values of COF are in harmony with the Johnson's theory which signifies that instances of pure ploughing are associated with $\mu < 0.3$ [35].

The results of this study go further and suggest that a transition from ploughing to cutting wear occurs when initial contacting pressures are furthermore increased either through higher loads or a reduced real contact area, relating COF values of 0.05 to unconstrained plastic flow during sliding. These findings were confirmed by SEM analysis, see Section 3.3.

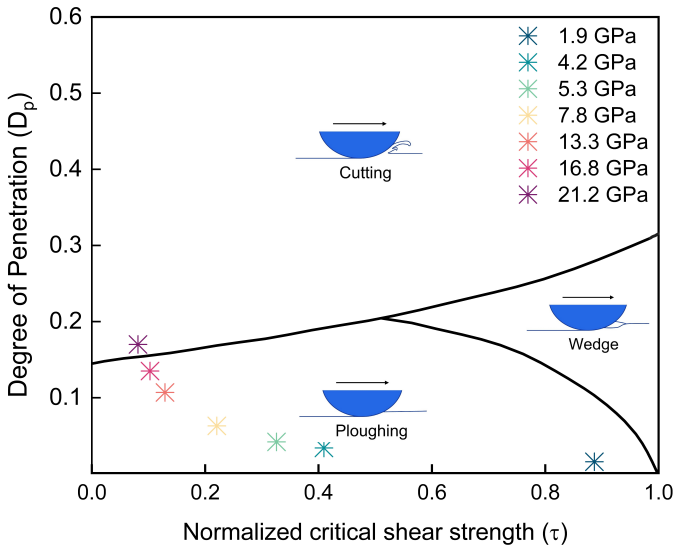

Figure 5: The wear map of ductile metals shows three distinct mechanisms of abrasive wear. Each star sign indicates a predictive wear mechanism according to the normalised shear strength between the contact and bulk shear strength, degree of penetration, and initial contact pressures.

3.3. Surface analysis

Figure 6 shows SEM analysis of the wear scar for all the CoCrMo surfaces after sliding for 2700 cycles in PBS under loads 10 mN to 200 mN for the macro and micro contact. Different wear mechanisms from mechanical to corrosive have been observed, for high and low initial contact pressures.

The sample tested under F_{n}=10 mN with D_{tip200} Figure (6a), showed no visible wear scar. However, plastic deformation is expected according to the Tresca criterion which states that yielding occurs when initial shear stress overcome the shear strength of the material. Considering initial penetration depth for this particular test calculated at (h=0.02 μm), along with the observed current alternation during rubbing suggests that the tip primarily disturbed the oxide layer, thought to be 1-4 nm thick [37], thereby exposing the bulk material to corrosion rather than inducing significant plastic deformation. Applying Archards law of wear for this testing condition suggests that the mechanical wear volume loss is present ($\mathrm{V_{mech}} = 0.00288$ $\mu\mathrm{m}^3$) but is nearly negligible compared to the corrosive wear volume loss ($\mathrm{V_{chem}} = 154.536$ $\mu\mathrm{m}^3$). Both values are presented in the supplementary material.

SEM images of all other surfaces confirm plastic deformation (Figure (6b-g)). From the observations made ploughing wear became evident for all surfaces tested with the micro-tip D_{tip25} (Figure (6d-g)). This supports the finding of Mace and Gilbert which has similarly reported excessive fretting depth and ploughing within a few hundred cycles under micro contacts [38]. Furthermore, SEM images (Figure (6d-g)) show the presence of 45° twinning lines on the sides of the wear scar. It is noteworthy that twinning became apparent only when the applied contacting pressures surpassed the material's hardness at 5.2 GPa. Furthermore, for samples tested under loads 200 mN and 100 mN with D_{tip25}, severe damage in the form of cracks were seen

along the wear scar (Figure (6f-g)). The substantial deformation evident on the surfaces usually coupled with the generation of chips and particles during these processes, results from the transition of wear mechanisms from ploughing to cutting wear [39]. A study by Mahato et. al., have linked similar surface features to plastic flow and the evolution of elevations in the surface ahead of the wedge during continued sliding [39]. Over time, these elevations increase in height and move closer together, eventually interacting to form a self-contact, known as a fold. As a fold exits in the contact region, through sliding it splits resulting in wear particles, leaving behind crack- and tear-like features on the surface.

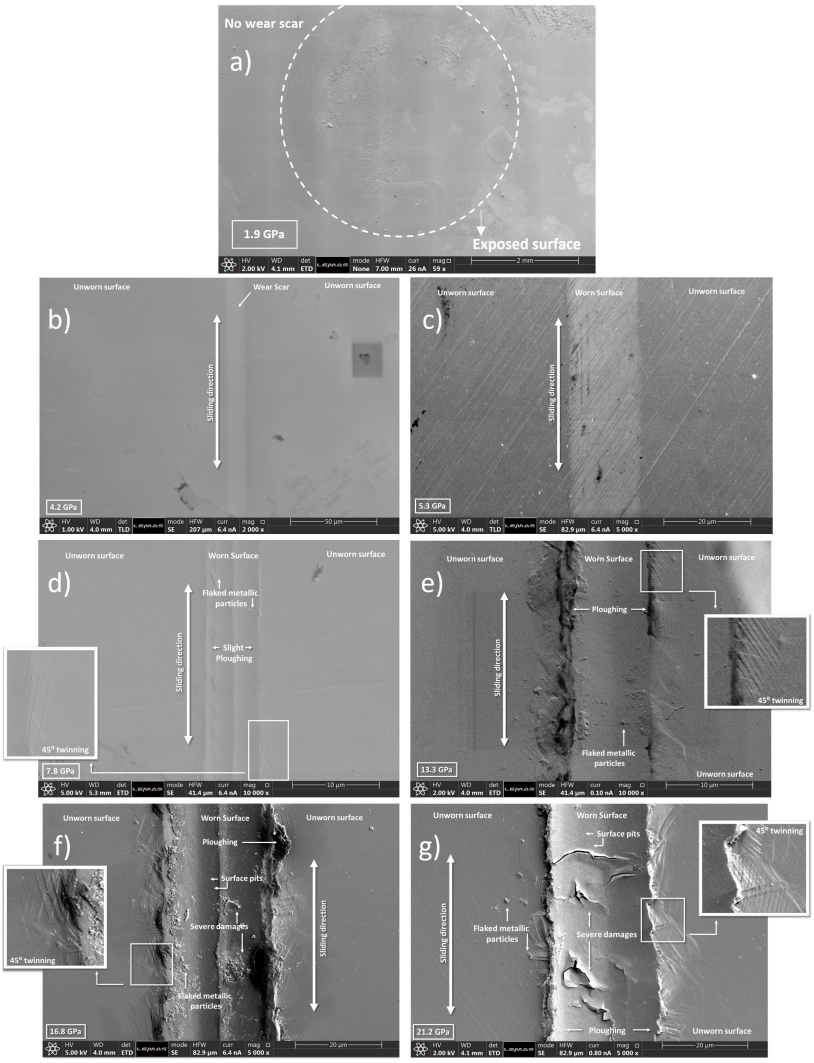

Figure 6: SEM Images of the wear scar under a) 1.9 GPa initial contact pressure obtained with a D_{tip200} and 10 mN where no wear scar was observed. b-c) 4.2 GPa and 5.3 GPa initial contact pressure obtained with D_{tip200} and a load of 100 mN and 200 mN respectively. Neither ploughing nor twinning was observed in those samples. d-e) 7.8 GPa and 13.3 GPa initial contact pressure obtained with D_{tip25} and a load of 10 mN and 50 mN respectively. Showing ploughing as the main wear mechanism and 45° twinning. f-g)16.8 GPa and 21.2 GPa initial contact pressure obtained with D_{tip25} and a load of 100 mN and 200 mN respectively. Shows severe damage, micro cracking and ploughing, as well as 45° twinning on the side of the wear scar.

3.4. Wear analysis

As outlined in Section 2.5, the acquired charge value Q was employed in Faraday's Law to obtain V_{chem}. In this study, the process involves fitting a line to the current data and integrating the area between the fitted line and the actual current curve, as shown in Figure 2b. Corrosion in passive regions is negligible compared to the corrosion in depassivated areas [40; 41]. However, in small contact areas, this difference becomes more significant. If corrosion in passive areas is also considered, the estimated corrosion wear would be higher than mechanical wear, as the total exposed surface area to corrosion is significantly larger than the localised contact area of the scratching tip. This overestimation occurs because the passive regions contribute additional net anodic current, whereas the actual wear process is confined to the much smaller contact zone. For example, $I_p A_p > I_a A_p$. Thus, determining Q requires integrating the current recorded during rubbing and subtracting the background current in passive areas. Further, subtraction of V_{chem} from V_{total} allowed for the determination of V_{mech}.

Based on the total volume loss measured by VSI it is apparent that an increase in contact pressure correlates with a rise in total wear volume loss (Figure 7a).

Figure 7b-c presents an analysis of the contribution of volume loss attributed to mechanical (V_{mech}) and corrosive (V_{chem}) processes in relation to the overall tribocorrosive volume loss (V_{total}), considering varying contact pressures.

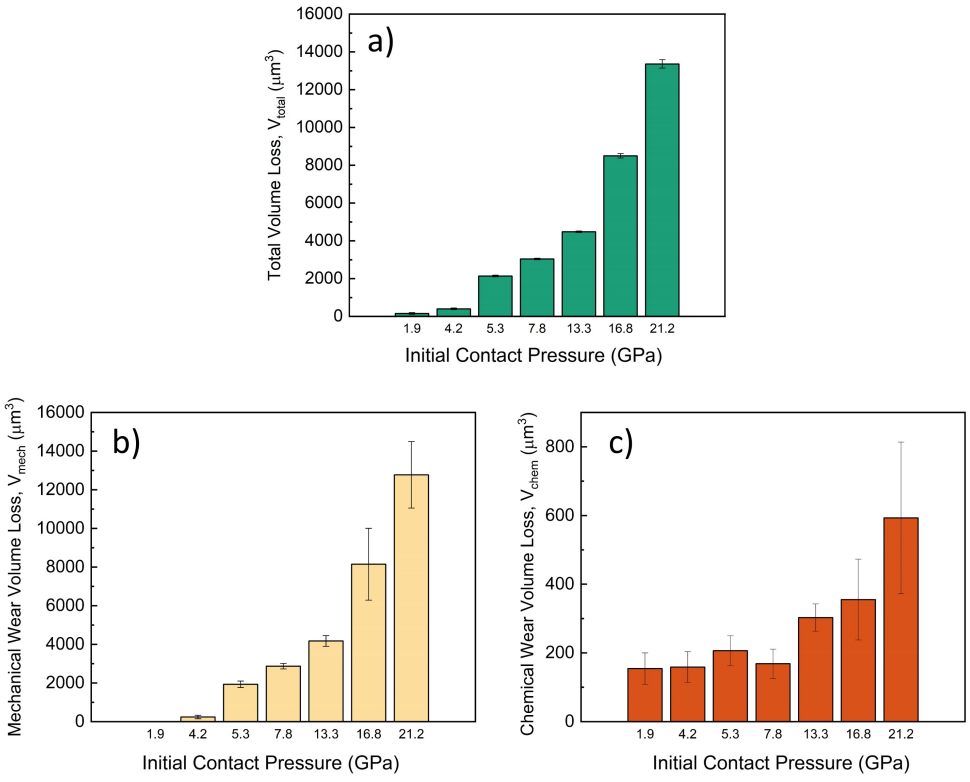

Figure 7: Graphs showing a) Total wear volume loss measured by VSI, b) Mechanical wear and c) Corrosive wear, under each initial contact pressure.

The data indicates a prevalent influence of mechanical wear over corrosive wear with the micro contact (D_{tip25}). However, this predominance gradually diminishes as the surface pressures decrease, reaching a critical point for the sample tested at 1.9 GPa, where corrosive wear surpasses mechanical wear.

The relative prevalence of each mechanism is shown in Figure 8a, showing the percentage attributed to the individual mechanisms. A larger real contacting area exposed a greater surface to the corrosive environment, leading to an augmented volume loss due to corrosion. This observation aligns with the findings of Mischler et al. [42], where their work reported an augmentation in the current corresponding correlation to a broader wear scar. As such, results show that CoCrMo alloys behave differently under micro and macro contact conditions due to pressure variations.

Figure 8b shows the boundary of the transition between different wear regimes as a function of the initial contact pressure and shear stress in CoCrMo alloys. When the shear stress falls below the materials shear strength (0.89 GPa), the figure shows that wear is entirely corrosion-driven. In this regime, the surface does not experience plastic deformation, and mechanical wear mechanisms are inactive. As the shear stress increases beyond the shear strength but initial contact pressures remains below the materials hardness (5.2 GPa), the figure illustrates the emergence of a mixed wear regime. In this intermediate zone, both mechanical and corrosive wear mechanisms contribute to material loss. Depending on the specific contact pressure within this range, either mechanism may dominate; however, both are actively involved in the degradation process. Once the contact pressure exceeds the hardness of the material, the figure shows that mechanical wear dominates. The wear mechanisms shift decisively toward severe material removal through ploughing and cutting. In this high-pressure regime, mechanical wear becomes the primary mode of material degradation, thus the contribution of corrosive wear becomes negligible.

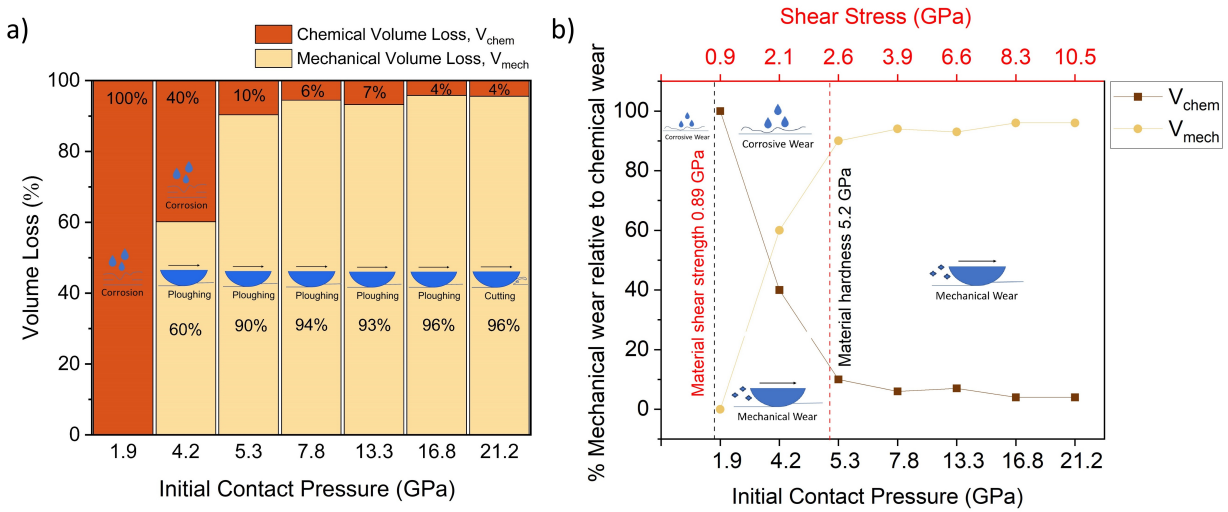

Figure 8: a) Graphs showing the percentage between mechanical and corrosive wear for all initial contact pressures. The icons represent the dominant wear type. b) Graph showing the boundaries between corrosion-dominated, mixed, and mechanical-dominated wear as a function of initial contact pressure and shear stress.

The results indicate that the variation in wear mechanisms at different scales could be a potential explanation to the differing size distributions of debris observed in scratch tests compared to simulator-generated debris [43]. This is highly important considering that it is well recognised that different types of debris trigger distinct ion release and inflammatory responses [44] . A comprehensive understanding of wear mechanisms across different scales, and their interconnected influence on wear particle formation and morphology, is crucial for optimising the wear behaviour of implants. Therefore this knowledge is essential for enhancing the longevity of orthopaedic devices and significantly improving patient outcomes.

4. Conclusion

This study comprehensively investigated the impact of macro and micro contact scales and shear stresses on the tribocorrosive behaviour of CoCrMo alloy. The research findings have led to the following conclusions:

- This study has demonstrated a significant correlation between the initial contact pressure and the tribological behaviour of the CoCrMo alloy. The findings underscore that the initial contact pressure at the real contact are a critical determinant in influencing material behaviour and wear mechanisms.

- The results have demonstrated that mechanical wear remains the predominant wear mechanism up to a critical transition point. The transition occurs when the applied shear stress approaches the material's inherent shear strength. At this point, the material can withstand the mechanical stresses without experiencing plastic deformation. Consequently, the contribution of mechanical wear diminishes, facilitating a transition to corrosion-dominated degradation.

- COF as low as 0.05 were linked to rapid asperity shake-down and unconstrained plastic flow for micro scale contacts, causing the material to deform easily. This process results in severe mechanical wear, characterised by the formation of cracks and significant surface damage. Such wear profoundly undermines the materials structural integrity and functional performance.

- Based on the SEM images and the tribocorrosive response of CoCrMo, this study suggests that debris size distribution and morphology are dependent on contact pressure, which in turn is influenced by the contact scale and load.

These insights underscore the importance of optimising contact conditions and surface interactions to enhance the durability and performance of biomedical implants. We show that controlling localised stresses can prevent transitions into damaging wear regimes, such as abrasive-dominated degradation. This insight supports specific design strategies such as optimising surface curvature, contact geometry, and surface finishing, to better distribute load and reduce peak stresses. In turn, this helps minimise the generation of wear particles, reducing the risk of osteolysis, and ultimately reducing the likelihood of implant loosening over time.

In addition, the results contribute to the development of predictive models for degradation behaviour by establishing a clear link between contact scale, pressure, and dominant wear mechanisms. Given that material performance was shown to be strongly scale-dependent, we recommend that standardisation authorities incorporate multiscale tribocorrosion testing protocols when evaluating biomaterials for implant use, as current single-scale approaches may overlook critical degradation modes relevant to in vivo conditions.

Further studies focussing on microstructural changes and their impact on particle formation and morphology are suggested to deepen our understanding of the impact of degradation mechanisms to improve the longevity of joint implants.

5. Acknowledgments

The authors acknowledge the technical staff at the School of Mechanical Engineering for their essential contributions to the experimental components of this research. Their support and expertise are greatly appreciated. The authors also express their gratitude to the technicians at the Leeds Electron Microscopy and Spectroscopy Centre (LEMAS) for their assistance with advanced microscopy and spectroscopy techniques, which were crucial to the successful completion of this work.

6. Funding

The BioTrib ETN project has received funding from the European Unions Horizon 2020 Research and Innovation Programme under Grant Agreement No. 956004.

7. Declaration

The authors declared no potential conflicts of interest with respect to the research, authorship, and/or publication of this article.

References

[1] T. Fretwurst, K. Nelson, D. Tarnow, H.-L. Wang, and W. Giannobile, "Is Metal Particle Release Associated with Peri-implant Bone Destruction? An Emerging Concept," *Journal of Dental Research*, vol. 97, pp. 259–265, 3 2018.

[2] D. Bitar, "Biological response to prosthetic debris," *World Journal of Orthopedics*, vol. 6, no. 2, p. 172, 2015.

[3] J.-D. Chang, S.-S. Lee, M. Hur, E.-M. Seo, Y.-K. Chung, and C.-J. Lee, "Revision Total Hip Arthroplasty in Hip Joints With Metallosis," *The Journal of Arthroplasty*, vol. 20, pp. 568–573, 8 2005.

[4] Fortune Business Insights, "The global hip replacement market size was valued at $7.42 billion in 2022 & is projected to grow from $7.72 billion in 2023 to $10.79 billion by 2030," tech. rep., Fortune Business Insights, 2023.

[5] M. T. Mathew, J. J. Jacobs, and M. A. Wimmer, "Wear-Corrosion Synergism in a CoCrMo Hip Bearing Alloy Is Influenced by Proteins," *Clinical Orthopaedics & Related Research*, vol. 470, pp. 3109–3117, 11 2012.

[6] K. Ghadirinejad, C. W. Day, R. Milimonfared, M. Taylor, L. B. Solomon, and R. Hashemi, "Fretting Wear and Corrosion-Related Risk Factors in Total Hip Replacement: A Literature Review on Implant Retrieval Studies and National Joint Replacement Registry Reports," *Prosthesis*, vol. 5, pp. 774–791, 8 2023.

[7] Y. Yan, A. Neville, and D. Dowson, "Biotribocorrosionan appraisal of the time dependence of wear and corrosion interactions: I. The role of corrosion," *Journal of Physics D: Applied Physics*, vol. 39, pp. 3200–3205, 8 2006.

[8] M. A. Wimmer, A. Fischer, R. Büscher, R. Pourzal, C. Sprecher, R. Hauert, and J. J. Jacobs, "Wear mechanisms in metal-on-metal bearings: The importance of tribochemical reaction layers," *Journal of Orthopaedic Research*, pp. n/a–n/a, 2009.

[9] A. Fischer, S. Weiß, and M. A. Wimmer, "The tribological difference between biomedical steels and CoCrMo-alloys," *Journal of the Mechanical Behavior of Biomedical Materials*, vol. 9, pp. 50–62, 5 2012.

[10] A. R. Beadling, M. G. Bryant, D. Dowson, and A. Neville, "Adverse loading effects on tribocorrosive degradation of 28 mm metal-on-metal hip replacement bearings," *Proceedings of the Institution of Mechanical Engineers, Part J: Journal of Engineering Tribology*, vol. 235, pp. 2664–2674, 12 2021.

[11] W. R. Chang, I. Etsion, and D. B. Bogy, "An Elastic-Plastic Model for the Contact of Rough Surfaces," *Journal of Tribology*, vol. 109, pp. 257–263, 4 1987.

[12] J. A. Greenwood and J. H. Tripp, "The Contact of Two Nominally Flat Rough Surfaces," *Proceedings of the Institution of Mechanical Engineers*, vol. 185, pp. 625–633, 6 1970.

[13] J. A. Greenwood and J. B. P. Williamson, "Contact of nominally flat surfaces," *Proceedings of the Royal Society of London. Series A. Mathematical and Physical Sciences*, vol. 295, pp. 300–319, 12 1966.

[14] A. Ghanbarzadeh, F. Motamen Salehi, M. Bryant, and A. Neville, "Modelling the evolution of electrochemical current in potentiostatic condition using an asperity-scale model of tribocorrosion," *Biotribology*, vol. 17, pp. 19–29, 3 2019.

[15] O. Brazil, J. B. Pethica, and G. M. Pharr, "The contribution of plastic sink-in to the static friction of single asperity microscopic contacts," *Proceedings of the Royal Society A: Mathematical, Physical and Engineering Sciences*, vol. 477, 12 2021.

[16] A. Mace and J. L. Gilbert, "Micro asperity-based fretting corrosion of CoCrMo, Ti-6Al-4V, and 316L SS: Assessment of an electrochemical and micro-mechanical model," *Tribology International*, vol. 180, p. 108222, 2 2023.

[17] The American Society for Testing and Materials, "Standard Specification for Wrought Cobalt-28Chromium-6Molybdenum Alloys for Surgical Implants (UNS R31537, UNS R31538, and UNS R31539)," tech. rep., ASTM International, 2020.

[18] "ISO 7206-2:2011/Amd 1:2016 Implants for surgery Partial and total hip joint prostheses Part 2: Articulating surfaces made of metallic, ceramic and plastics materials Amendment 1," 2016.

[19] Y. Liu, A. Mace, H. Lee, M. Camargo, and J. L. Gilbert, "Single asperity sub-nano to nanoscale wear and tribocorrosion of wrought CoCrMo and additively manufactured CoCrMoW alloys," *Tribology International*, vol. 174, p. 107770, 10 2022.

[20] J. Lanigan, S. Fatima, T. Charpentier, A. Neville, D. Dowson, and M. Bryant, "Lubricious ionic polymer brush functionalised silicone elastomer surfaces," *Biotribology*, vol. 16, pp. 1–9, 12 2018.

[21] R. Silva, M. D. d. Santos, R. Madureira, R. Soares, R. Neto, . A. Vieira, P. A. R. Gonçalves, P. M. S. M. Leite, L. Vieira, and F. Viana, "Scratch and Wear Behaviour of Co-Cr-Mo Alloy in Ringers Lactate Solution," *Materials*, vol. 16, p. 2923, 4 2023.

[22] R. Ahmed, H. de Villiers Lovelock, N. Faisal, and S. Davies, "Structureproperty relationships in a CoCrMo alloy at micro and nano-scales," *Tribology International*, vol. 80, pp. 98–114, 12 2014.

[23] B. N. J. Persson, "Area of Real Contact: Elastic and Plastic Deformations," pp. 45–91, Springer Berlin Heidelberg, 2000.

[24] A. Tiwari, A. Almqvist, and B. N. J. Persson, "Plastic Deformation of Rough Metallic Surfaces," *Tribology Letters*, vol. 68, p. 129, 12 2020.

[25] Vanesa Martínez Nogués and R. B. Cook Martin Stolz Robert J K Wood, *Nano-scale tribocorrosion of CoCrMo biomedical alloys*. PhD thesis, UNIVERSITY OF SOUTHAMPTON, 2016.

[26] A. Hodgson, S. Kurz, S. Celene Virtanen, V. Fervel, and C. Olsson, "Passive and transpassive behavior of CoCrMo in simulated biological solutions," *Electrochimica Acta*, 2004.

[27] A. S. Hammood, L. Thair, H. D. Altawaly, and N. Parvin, "Tribocorrosion Behaviour of Ti6Al4V Alloy in Biomedical Implants: Effects of Applied Load and Surface Roughness on Material Degradation," *Journal of Bio- and Tribo-Corrosion*, vol. 5, p. 85, 12 2019.

[28] B. J. Hamrock and D. Dowson, "ISOTHERMAL ELASTOHYDRODYNAMIC LUBRICATION OF POINT CONTACTS - 4. STARVATION RESULTS.," in *American Society of Mechanical Engineers (Paper)*, no. 76 -Lub-31, 1976.

[29] D. Landolt, S. Mischler, and M. Stemp, "Electrochemical methods in tribocorrosion: a critical appraisal," *Electrochimica Acta*, vol. 46, pp. 3913–3929, 8 2001.

[30] M. Taufiqurrakhman, A. Neville, and M. G. Bryant, "The Effect of Protein Structure and Concentration on Tribocorrosion and Film Formation on CoCrMo Alloys," *Journal of Bio- and Tribo-Corrosion*, vol. 7, p. 147, 12 2021.

[31] V. L. Popov, M. Heß, and E. Willert, *Handbook of Contact Mechanics*. Berlin, Heidelberg: Springer Berlin Heidelberg, 2019.

[32] C. M. Mate and R. W. Carpick, *Tribology on the Small Scale*. Oxford University PressOxford, 8 2019.

[33] D. Landolt and S. Mischler, *Tribocorrosion of Passive Metals and Coatings*. Landolt2011, 2011.

[34] F. P. Bowden, A. J. W. Moore, and D. Tabor, "The Ploughing and Adhesion of Sliding Metals," *Journal of Applied Physics*, vol. 14, pp. 80–91, 2 1943.

[35] K. L. Johnson, *Contact Mechanics*. Cambridge University Press, 5 1985.

[36] P. Somasundaran and A. T. Hubbard, *ENCYCLOPEDIA OF Surface and Colloid Science*. Boca Raton: CRC Press, 11 2015.

[37] D. Sun, J. Wharton, R. Wood, L. Ma, and W. Rainforth, "Microabrasioncorrosion of cast CoCrMo alloy in simulated body fluids," *Tribology International*, vol. 42, pp. 99–110, 1 2009.

[38] A. Mace and J. L. Gilbert, "Micro-asperity tribocorrosion of CoCrMo, Ti6Al4V, and 316 stainless steel in air and physiological solution: Small scale reciprocal sliding of a single diamond tip," *Wear*, vol. 498-499, p. 204332, 6 2022.

[39] A. Mahato, Y. Guo, H. Yeung, and S. Chandrasekar, "Surface flow in severe plastic deformation of metals by sliding," *IOP Conference Series: Materials Science and Engineering*, vol. 63, p. 012016, 8 2014.

[40] S. Mischler, A. Spiegel, and D. Landolt, "The role of passive oxide films on the degradation of steel in tribocorrosion systems," *Wear*, vol. 225-229, pp. 1078–1087, 4 1999.

[41] A. Igual Munoz, N. Espallargas, and S. Mischler, "Tribocorrosion: Definitions and Relevance," pp. 1–6, 2020.

[42] S. Mischler and A. I. Muñoz, "Wear of CoCrMo alloys used in metal-on-metal hip joints: A tribocorrosion appraisal," *Wear*, vol. 297, pp. 1081–1094, 1 2013.

[43] R. Pourzal, I. Catelas, R. Theissmann, C. Kaddick, and A. Fischer, "Characterization of wear particles generated from CoCrMo alloy under sliding wear conditions," *Wear*, vol. 271, no. 9-10, pp. 1658–1666, 2011.

[44] M. S. Caicedo, L. Samelko, K. McAllister, J. J. Jacobs, and N. J. Hallab, "Increasing both CoCrMo-alloy particle size and surface irregularity induces increased macrophage inflammasome activation in vitro potentially through lysosomal destabilization mechanisms," *Journal of Orthopaedic Research*, vol. 31, no. 10, pp. 1633–1642, 2013.